Solar Orbiter First Results (Cruise Phase)

The angular-momentum flux in the solar wind observed during Solar Orbiter's first orbit

Daniel Verscharen[1,2] , David Stansby[1], Adam J. Finley[3], Christopher J. Owen[1], Timothy Horbury[4],
Milan Maksimovic[5], Marco Velli[6], Stuart D. Bale[4,7,8,9], Philippe Louarn[10], Andrei Fedorov[10], Roberto Bruno[11],
Stefano Livi[12], Yuri V. Khotyaintsev[13], Antonio Vecchio[5,14], Gethyn R. Lewis[1], Chandrasekhar Anekallu[1],
Christopher W. Kelly[1], Gillian Watson[1], Dhiren O. Kataria[1], Helen O'Brien[4], Vincent Evans[4],
Virginia Angelini[4], and the Solar Orbiter SWA, MAG and RPW teams

[1] Mullard Space Science Laboratory, University College London, Holmbury House, Holmbury St. Mary, Dorking RH5 6NT, UK
   e-mail: d.verscharen@ucl.ac.uk
[2] Space Science Center, University of New Hampshire, Durham, NH 03824, UK
[3] Department of Astrophysics-AIM, University of Paris-Saclay and University of Paris, CEA, CNRS, 91191 Gif-sur-Yvette Cedex,
   France
[4] Department of Physics, The Blackett Laboratory, Imperial College London, London SW7 2AZ, UK
[5] LESIA, Observatoire de Paris, Université PSL, CNRS, Sorbonne Université, Université de Paris, 5 place Jules Janssen,
   92195 Meudon, France
[6] Department of Earth, Planetary, and Space Sciences, University of California Los Angeles, Los Angeles, CA 90095, USA
[7] Physics Department, University of California, Berkeley, CA 94720, USA
[8] Space Sciences Laboratory, University of California, Berkeley, CA 94720, USA
[9] School of Physics and Astronomy, Queen Mary University of London, London E1 4NS, UK
[10] Institut de Recherche en Astrophysique et Planétologie, 31028 Toulouse Cedex 4, France
[11] INAF-Istituto di Astrofisica e Planetologia Spaziali, 00133 Roma, Italy
[12] Southwest Research Institute, San Antonio, TX 78238, USA
[13] Swedish Institute of Space Physics (IRF), Box 537, 751 21 Uppsala, Sweden
[14] Radboud Radio Lab., Department of Astrophysics/IMAPP-Radboud University, PO Box 9010, 6500 GL Nijmegen,
   The Netherlands

ABSTRACT

Aims. We present the first measurements of the angular-momentum flux in the solar wind recorded by the Solar Orbiter spacecraft. Our aim is to validate these measurements to support future studies of the Sun's angular-momentum loss.
Methods. We combined 60-min averages of the proton bulk moments and the magnetic field measured by the Solar Wind Analyser and the magnetometer onboard Solar Orbiter. We calculated the angular-momentum flux per solid-angle element using data from the first orbit of the mission's cruise phase in 2020. We separated the contributions from protons and from magnetic stresses to the total angular-momentum flux.
Results. The angular-momentum flux varies significantly over time. The particle contribution typically dominates over the magnetic-field contribution during our measurement interval. The total angular-momentum flux shows the largest variation and is typically anti-correlated with the radial solar-wind speed. We identify a compression region, potentially associated with a co-rotating interaction region or a coronal mass ejection, which leads to a significant localised increase in the angular-momentum flux, albeit without a significant increase in the angular momentum per unit mass. We repeated our analysis using the density estimate from the Radio and Plasma Waves instrument. Using this independent method, we find a decrease in the peaks of positive angular-momentum flux, but otherwise, our results remain consistent.
Conclusions. Our results largely agree with previous measurements of the solar wind's angular-momentum flux in terms of amplitude, variability, and dependence on radial solar-wind bulk speed. Our analysis highlights the potential for more detailed future studies of the solar wind's angular momentum and its other large-scale properties with data from Solar Orbiter. We emphasise the need for studying the radial evolution and latitudinal dependence of the angular-momentum flux in combination with data from Parker Solar Probe and other assets at heliocentric distances of 1 au and beyond.

Key words. magnetohydrodynamics (MHD) – plasmas – Sun: magnetic fields – solar wind – stars: rotation

1. Introduction

The solar corona expands into interplanetary space in the form of the solar wind (Parker 1958; Neugebauer & Snyder 1962; Verscharen et al. 2019). In this process, the solar wind plasma removes mass, momentum, energy, and angular momentum

from the Sun. In the lower corona, the Sun's magnetic field forces the plasma into a quasi-rigid co-rotation with the photosphere, following the co-rotation of the field's photospheric footpoints. With increasing distance from the photosphere, the torque exerted by the coronal magnetic field on the plasma decreases (Weber & Davis 1967). In this way, the large-scale

magnetic field mediates a smooth transition from co-rotation to quasi-radial expansion. Therefore, the solar wind is not "flung" from the photosphere on a ballistic trajectory, which would lead to a torque-free azimuthal velocity profile taking the following form:

$$U_\phi(r) \simeq \frac{R_\odot^2 \Omega_\odot \sin\theta}{r}, \qquad (1)$$

where $R_\odot$ is the solar radius, $\Omega_\odot$ is the Sun's angular rotation frequency, θ is the co-latitude, and r is the heliocentric distance. Instead, the solar wind experiences a significant torque in its acceleration region at even larger distances from the photosphere, leading to greater azimuthal speeds than predicted by Eq. (1). In turn, the torque applied to the Sun by the magnetic field in this process slows down the Sun's rotation on long time scales (Mestel 1968; Reiners & Mohanty 2012). Local measurements of the solar-wind angular-momentum flux provide an estimate for the global angular-momentum loss rate, which ultimately causes the rotation period of the Sun and, by extrapolation, of Sun-like stars on the main sequence to increase with age (Barnes 2003; Gallet & Bouvier 2013; Matt et al. 2015; Pantolmos & Matt 2017).

Measurements of the solar-wind angular-momentum flux are particularly challenging from an instrumental point of view. They require an accurate determination of the azimuthal component U_ϕ of the particle bulk velocity, which is typically more than one order of magnitude less than its radial component U_r. Nevertheless, early measurements of the solar wind already estimated its angular momentum (Hundhausen et al. 1970; Lazarus & Goldstein 1971; Pizzo et al. 1983; Marsch & Richter 1984). Modern space instrumentation provides us with higher spacecraft-pointing accuracy and, thus, a more accurate determination of U_ϕ. Moreover, as the average ratio U_ϕ/U_r increases with decreasing heliocentric distance, the error in the quantification of the angular-momentum flux is generally smaller when measured at smaller distances from the Sun (Finley et al. 2020, 2021). In addition, co-rotating interaction regions have not yet formed (Richter & Luttrell 1986; Allen et al. 2020) and interplanetary coronal mass ejections have not expanded enough to disturb nearby wind streams (Möstl et al. 2020) at small distances from the Sun. Therefore, near-Sun measurements enable the sampling of more pristine and less processed solar wind. Solar Orbiter and Parker Solar Probe share the advantages of both modern space instrumentation and an orbit that leads them close to the Sun (Fox et al. 2016; Müller et al. 2020). We present the first observations of the solar wind's angular-momentum flux observed by Solar Orbiter during the first orbit of its cruise phase in 2020.

2. Data analysis

We analyse a combined set of data from the Proton-Alpha Sensor (PAS) of Solar Orbiter's Solar Wind Analyser (SWA, Owen et al. 2020) suite and from Solar Orbiter's fluxgate magnetometer (MAG, Horbury et al. 2020). Our dataset includes all time intervals from 2020-07-07 until 2020-10-27, for which both SWA/PAS and MAG data are available. We ignore all other intervals and those in which the quality flags for either dataset indicate poor data quality (we only include data with a quality flag of 3). After this selection, we thus retain about 38.9% of the total time interval in our dataset (for time coverage, see also Fig. 1). During this time, Solar Orbiter recorded data at heliocentric distances between 0.591 and 0.989 au. The time average of the spacecraft's heliocentric distance in our dataset is 0.851 au.

The calculation of the angular-momentum flux is very sensitive to uncertainties in the direction of the bulk velocity and in the direction of the magnetic field. The finite angular resolution of PAS introduces an uncertainty in the knowledge of the bulk-speed direction. The calibration accuracy of PAS is $\lesssim 1°$. The pointing knowledge of the MAG sensor is largely determined by the uncertainty of the spacecraft's boom deployment angle. It introduces an angular uncertainty of the magnetic-field measurement of $\lesssim 1°$. Planned inter-instrument alignment reconstructions of the boom orientation will become feasible in the future once the instruments have recorded sufficient amounts of data for a large statistical analysis (Walsh et al. 2020). For solar wind speeds above $300\,\mathrm{km\,s^{-1}}$, the relative uncertainty of the SWA/PAS speed measurement due to counting statistics is less than 1%. The relative uncertainty of the density measurement is energy-dependent with a maximum of 20%, which we apply as a conservative estimate to our entire dataset. At very low energies (corresponding to solar-wind speeds below $\sim 300\,\mathrm{km\,s^{-1}}$), the sensitivity decreases further so that additional correction factors are required, which have not yet been conclusively determined. The expected MAG offset is $\sim \pm 0.1$ nT, which we take as the absolute uncertainty of our individual magnetic-field component measurements. The requirement of the absolute knowledge error of the spacecraft pointing is ≤ 3 arcmin (García Marirrodriga et al. 2021), which is mostly driven by the instrument requirements of the remote-sensing suite and a minor contributor to the pointing knowledge uncertainties for our study.

We base our analysis on the PAS normal-mode ground moments integrated from the proton part (core and beam) of the full three-dimensional measured ion distributions and the MAG normal-mode vectors of the magnetic field. In normal mode, the PAS ground moments are available every four seconds, while the MAG vectors are available with a cadence of 8 vectors per second. We merge and average both data products over intervals of 60 min to reduce any natural fluctuations in the data due to, for example, waves and turbulence, as we are interested in the angular-momentum flux of the bulk solar wind. Our selection and averaging procedure leaves us with 1036 individual data points.

The angular momentum is contained in the mechanical flux of the solar-wind particles. In addition, there is transport of angular momentum due to magnetic-field stresses. Ignoring anisotropies in the particle distributions and contributions from particles other than protons[1], the total angular-momentum flux is thus the sum of the proton and magnetic-field terms (see Marsch & Richter 1984). We define the total angular-momentum flux per solid-angle element in spherical heliocentric coordinates as:

$$\mathcal{F}_{\mathrm{tot}} = \mathcal{F}_p + \mathcal{F}_B, \qquad (2)$$

where

$$\mathcal{F}_p = r^3 \rho U_r U_\phi \qquad (3)$$

is the proton contribution to the angular-momentum flux, and

$$\mathcal{F}_B = -r^3 \frac{B_r B_\phi}{4\pi} \qquad (4)$$

is the contribution from magnetic stresses (in cgs units) to the angular-momentum flux, ρ is the proton mass density, $\boldsymbol{U}$ is the

---

[1] PAS has the capability to determine the moments of the solar-wind α-particle component as well. However, this dataset requires further calibration, so that we neglect α-particles at this point.
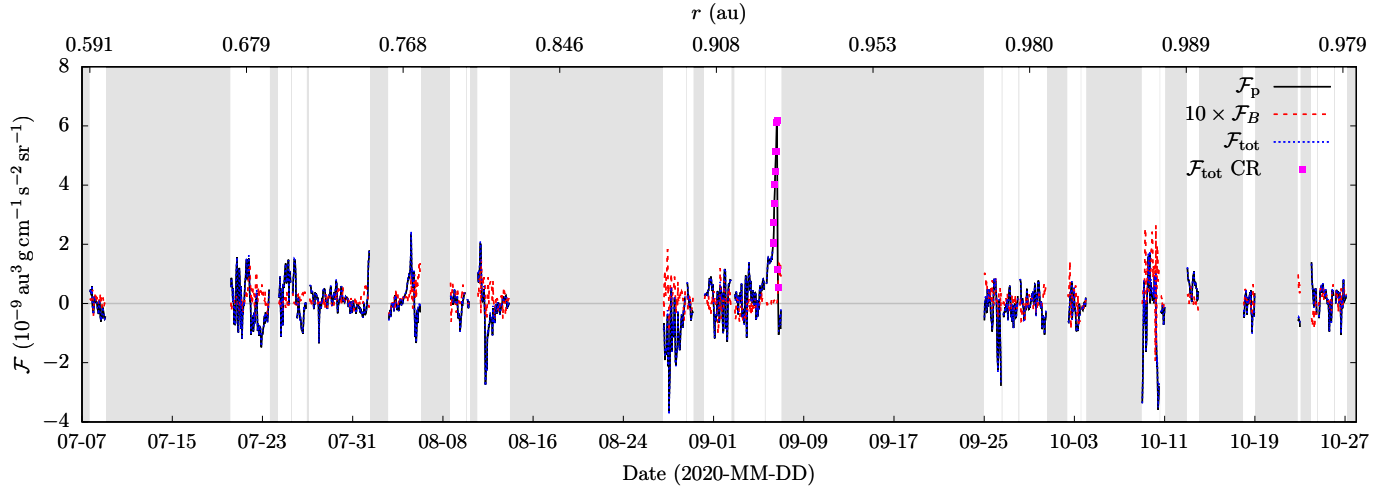
Fig. 1. Time series of the angular-momentum flux per solid-angle element measured during Solar Orbiter's first orbit of the cruise phase. The diagram shows the proton contribution $\mathcal{F}_p$, the magnetic-field contribution $\mathcal{F}_B$, and the sum of both, $\mathcal{F}_{tot}$. In order to increase the visibility, we multiply $\mathcal{F}_B$ with a factor 10. The magenta squares represent the measurements of $\mathcal{F}_{tot}$ during the time of the compression region (CR) on 2020-09-06. The axis at the top indicates the heliocentric distance of the spacecraft at the time of the measurement. The scale of this axis is not linear. The grey-shaded areas indicate times for which our merged SWA/PAS-MAG data product is unavailable or the data flags for either dataset indicate poor data quality.

proton bulk velocity, and $\boldsymbol{B}$ is the magnetic field. The subscript r indicates the radial vector component, and the subscript ϕ indicates the azimuthal component in spherical heliocentric coordinates. We use our 60-min averages of the measured solar-wind parameters as the input for our calculations of $\mathcal{F}_p$ and $\mathcal{F}_B$ according to Eqs. (3) and (4). We recognise that our analysis represents only a first validation of methods to study angular-momentum flux with Solar Orbiter. Therefore, it ignores other contributions to the total angular-momentum flux (see Sect. 4), which must be investigated in future detailed studies.

3. Results

3.1. Timeseries and overview

Figure 1 shows the timeseries of $\mathcal{F}_p$, $\mathcal{F}_B$, and $\mathcal{F}_{tot}$ over the analysed data interval. Gaps in this plot represent data gaps or those intervals that we exclude according to our selection criteria. Figure 1 illustrates the natural variation of the angular-momentum flux over time, which is typically greater than its mean magnitude. Across all data points, the mean value of $\mathcal{F}_p$ is $2.29 \times 10^{-11} \, \mathrm{au}^3 \, \mathrm{g} \, \mathrm{cm}^{-1} \, \mathrm{s}^{-2} \, \mathrm{sr}^{-1}$, while the mean value of $\mathcal{F}_B$ is $1.72 \times 10^{-11} \, \mathrm{au}^3 \, \mathrm{g} \, \mathrm{cm}^{-1} \, \mathrm{s}^{-2} \, \mathrm{sr}^{-1}$. In general, $\mathcal{F}_p$ exhibits significantly more variation than $\mathcal{F}_B$. As expected for a conserved quantity, $\mathcal{F}_{tot}$ shows no secular dependence on heliocentric distance.

On 2020-09-06, we recorded a time interval of significantly increased $\mathcal{F}_p$ and $\mathcal{F}_{tot}$. Upon closer inspection, this interval corresponds to a time of increased ρ, probably associated with the compression in front of a co-rotating interaction region or a coronal mass ejection seen as a flux rope in the magnetic field. Due to this enhancement in ρ, the associated plasma carries more angular-momentum flux than the solar wind before or after the compression region. The compression region does not exhibit enhancements in U_r or U_ϕ (not shown here), suggesting that the compression region facilitates a similar angular-momentum flux per unit mass as the solar wind. Our results in Sect. 3.4 support this suggestion. We highlight the measurements taken during the
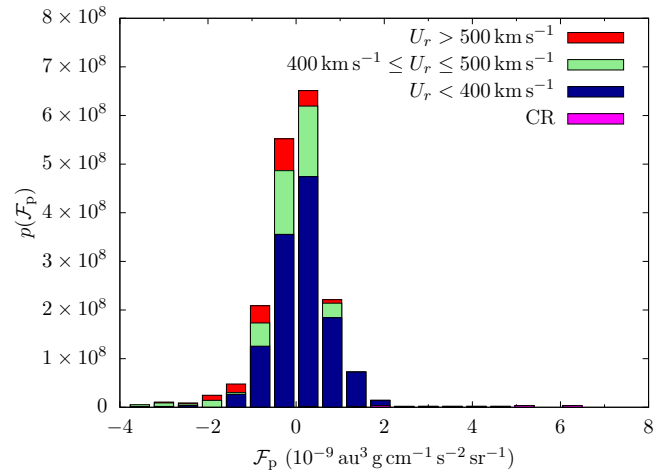

Fig. 2. Histogram of the proton contribution $\mathcal{F}_p$ to the solar wind's angular-momentum flux per solid-angle element. The vertical axis indicates the probability density of $\mathcal{F}_p$. We stack the histograms for fast ($U_r > 500 \, \mathrm{km} \, \mathrm{s}^{-1}$), intermediate ($400 \, \mathrm{km} \, \mathrm{s}^{-1} \leq U_r \leq 500 \, \mathrm{km} \, \mathrm{s}^{-1}$), and slow ($U_r < 400 \, \mathrm{km} \, \mathrm{s}^{-1}$) wind. The magenta areas represent the measurements of $\mathcal{F}_p$ during the time of the compression region (CR) on 2020-09-06.

time interval associated with this compression region in our figures as magenta squares.

3.2. Variability of the angular-momentum flux

In Figs. 2 and 3, we show histograms of the measured values of $\mathcal{F}_p$ and $\mathcal{F}_B$ for our dataset in terms of their probability distributions. We colour-code the contributions from fast, intermediate, and slow solar wind in our histograms. Due to the dominance of $\mathcal{F}_p$, the histogram of the probability distribution for $\mathcal{F}_{tot}$ (not shown) is almost identical to the histogram for $\mathcal{F}_p$. Both histograms reflect the broad variation in the angular-momentum flux and the range of observed values. According to Fig. 2, the majority of the distribution is centred around negative values of
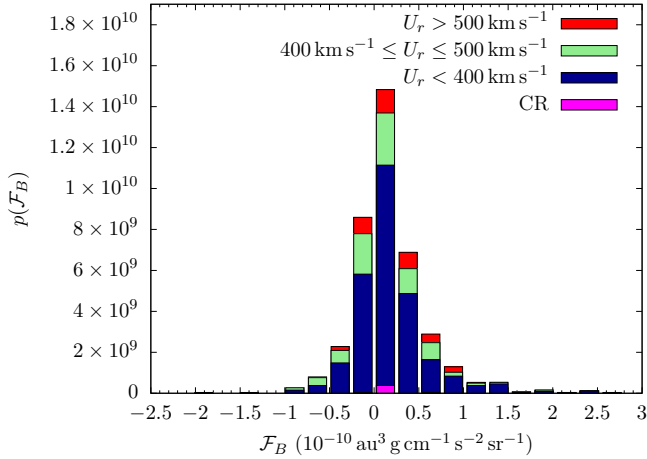
Fig. 3. Histogram of the magnetic-field contribution $\mathcal{F}_B$ to the solar wind's angular-momentum flux per solid-angle element. Details are the same as in Fig. 2.

$\mathcal{F}_p$, while the outliers at large $\mathcal{F}_p$ shift the mean of our measurements to $\mathcal{F}_p > 0$. These outliers are mostly associated with the compression region on 2020-09-06.

For a more quantitative statistical analysis, we list the mean values, the standard deviations, as well as the maximum and minimum values of $\mathcal{F}_p$, $\mathcal{F}_B$, and $\mathcal{F}_{tot}$ in Table 1. In addition, Table 1 provides these statistical markers separated by time intervals with $U_r < 400\,\mathrm{km\,s^{-1}}$ and $U_r > 500\,\mathrm{km\,s^{-1}}$ as a means to distinguish characteristic slow wind from fast wind, respectively. We find that $\mathcal{F}_p > 0$ and $\mathcal{F}_{tot} > 0$ in the observed slow-wind intervals ($U_r < 400\,\mathrm{km\,s^{-1}}$), while $\mathcal{F}_p < 0$ and $\mathcal{F}_{tot} < 0$ in the observed fast-wind intervals ($U_r > 500\,\mathrm{km\,s^{-1}}$). A similar behaviour has been seen in Parker Solar Probe measurements (Finley et al. 2021). In the separated data subsets for slow wind and fast wind, the mean values of $|\mathcal{F}_p|$ are greater than the mean value of $|\mathcal{F}_p|$ in our full dataset of all measurements. The means of $\mathcal{F}_B$ are positive, independent of our categorisation by wind speed, and the mean value of $\mathcal{F}_B$ in our slow-wind and fast-wind intervals is less than the mean value of $\mathcal{F}_B$ in all measurement intervals. We note, however, that the mean value of $\mathcal{F}_B$ is very small for the separated slow-wind and fast-wind intervals, so that this result is potentially not significant (see also Fig. 5).

3.3. Speed dependence of the angular-momentum flux

Figure 4 shows our measurements of $\mathcal{F}_p$ as a function of U_r. This visualisation confirms the significant U_r-dependence of the angular-momentum flux, which has been noted in previous studies and is discussed further in Sect. 4. The particle contribution to the angular-momentum flux shows a stronger relative variation in slow wind compared to fast wind. We also observe a trend towards negative values of $\mathcal{F}_p$ (and thus $\mathcal{F}_{tot}$) at larger U_r. Figure 5 shows the same but for $\mathcal{F}_B$. The magnetic-field contribution does not follow the same clear trend in its U_r-dependence as $\mathcal{F}_p$. Figures 4 and 5 include horizontal and vertical error bars to represent ΔU_r, $\Delta \mathcal{F}_p$, and $\Delta \mathcal{F}_B$. The error bars follow from error propagation of the individual measurement uncertainties quoted in Sect. 2, which corresponds to the application of the standard error of the mean based on the individual uncertainties. We find that, in our hourly averages, the relative errors ΔU_r, $\Delta \mathcal{F}_p$, and $\Delta \mathcal{F}_B$ are negligible.

A comparison of the magenta points in Figs. 4 and 5 reveals that $\mathcal{F}_B$ is not enhanced in the compression region compared to the time intervals outside the compression region. We note that the unit on the vertical axis in Fig. 5 is one order of magnitude smaller than the unit on the vertical axis in Fig. 4. This reflects again that $\mathcal{F}_p$ is on average the dominant contribution to $\mathcal{F}_{tot}$. In order to quantify the U_r-dependence, we apply least-squares Marquardt–Levenberg fits to our measurements according to the linear equation:

$$\mathcal{F} = aU_r + b, \tag{5}$$

with the fit parameters a and b, where $\mathcal{F}$ represents either $\mathcal{F}_p$, $\mathcal{F}_B$, or $\mathcal{F}_{tot}$. We show the resulting fit parameters including their errors in Table 2.

3.4. Mass-flux dependence of the angular-momentum flux

We define the proton mass flux per solid-angle element as:

$$\mathcal{G}_p = r^2 \rho U_r. \tag{6}$$

As $\mathcal{F}_p$ is carried by the proton flow, we combine $\mathcal{F}_p$ and $\mathcal{G}_p$ in Fig. 6 and analyse their dependence. We colour-code each measurement point with its associated value of U_r, which allows us to link Fig. 6 with Fig. 4. All time intervals with $\mathcal{G}_p \gtrsim 2 \times 10^{-15}\,\mathrm{au^2\,g\,cm^{-2}\,s^{-1}\,sr^{-1}}$ in our dataset exhibit $\mathcal{F}_p > 0$. The majority of these points correspond to the compression region on 2020-09-06. We highlight them as magenta squares in Fig. 6, illustrating that the mass-flux dependence is a useful method to separate transient and atypical plasma intervals from the regular background solar wind (see also Stansby et al. 2019).

The value of rU_ϕ is a measure of the local specific angular momentum per proton. Since $\mathcal{F}_p = rU_\phi \mathcal{G}_p$, isocontours of constant rU_ϕ correspond to bent curves when using a logarithmic $\mathcal{G}_p$-axis in Fig. 6. We show these isocontours as grey dashed curves for a range of rU_ϕ values from ± 10 to $\pm 40\,\mathrm{au\,km\,s^{-1}}$. At the low-$\mathcal{G}_p$ end, the distribution scatters almost symmetrically around a value of $\mathcal{F}_p = 0$. The envelope of the distribution in this $\mathcal{G}_p$ range follows isocontours of constant $\pm |rU_\phi|$, meaning that the scatter in $\mathcal{F}_p$ is well defined by a fixed range of constant magnitudes of the angular momentum per proton. At intermediate $\mathcal{G}_p$, the symmetry around $\mathcal{F}_p = 0$ breaks, and more data points occur at $\mathcal{F}_p > 0$. At $\mathcal{F}_p > 0$, the envelope of the data distribution in terms of rU_ϕ decreases as $\mathcal{G}_p$ increases in the intermediate-$\mathcal{G}_p$ range. The points representing the compression region largely lie on the same isocontours of rU_ϕ as the bulk of the slow solar wind. This behaviour suggests that the increase in $\mathcal{F}_p$ associated with the compression region is mostly due to an increase in ρ rather than to an increase in the specific angular momentum per proton compared to the regular slow wind.

3.5. Spectral analysis of the angular-momentum flux

Solar Orbiter's high temporal resolution in the measurement of both the particles and the magnetic field enables the analysis of the power spectrum of the variable angular-momentum flux over a wide range of frequencies. In order to demonstrate the suitability of Solar Orbiter data for future studies of this type, we present such a spectral analysis of the angular-momentum flux based on our dataset. We applied a non-uniform fast Fourier transform (Barnett et al. 2019; Barnett 2021) to the timeseries data of $\mathcal{F}_p$ and $\mathcal{F}_B$ throughout our entire dataset. For this calculation, we use 1-min averages of the data instead of the 60-min averages

Table 1. Statistical properties of $\mathcal{F}_\mathrm{p}$, $\mathcal{F}_B$, and $\mathcal{F}_\mathrm{tot}$ in our full dataset and split by radial solar-wind speed.

	Mean (10^{-11} au^3 g cm^{-1} s^{-2} sr^{-1})	Min (10^{-9} au^3 g cm^{-1} s^{-2} sr^{-1})	Max (10^{-9} au^3 g cm^{-1} s^{-2} sr^{-1})
All speeds			
$\mathcal{F}_\mathrm{p}$	2.29 ± 82.57	-3.66	6.19
$\mathcal{F}_B$	1.72 ± 4.16	-0.194	0.264
$\mathcal{F}_\mathrm{tot}$	4.01 ± 82.59	-3.75	6.19
$U_\mathrm{r} < 400\,\mathrm{km\,s}^{-1}$			
$\mathcal{F}_\mathrm{p}$	15.5 ± 81.2	-3.37	6.19
$\mathcal{F}_B$	0.923 ± 5.560	-0.230	0.254
$\mathcal{F}_\mathrm{tot}$	16.4 ± 81.0	-3.37	6.19
$U_\mathrm{r} > 500\,\mathrm{km\,s}^{-1}$			
$\mathcal{F}_\mathrm{p}$	-73.4 ± 119.8	-5.48	0.834
$\mathcal{F}_B$	0.593 ± 5.474	-0.174	0.101
$\mathcal{F}_\mathrm{tot}$	-72.8 ± 121.8	-5.49	0.868
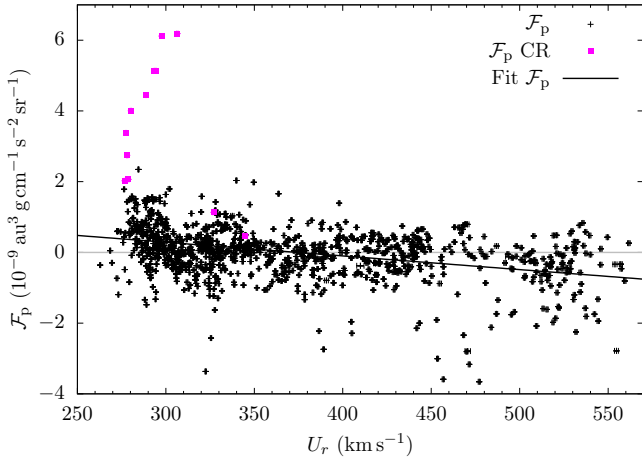
Fig. 4. Dependence of the proton contribution $\mathcal{F}_\mathrm{p}$ to the angular-momentum flux on the radial proton bulk speed U_r. We show the measurements of $\mathcal{F}_\mathrm{p}$ as points and overplot the linear fit to Eq. (5) as a black line. All measurement points have horizontal and vertical error bars, which are small due to the time-averaging. The fit parameters are given in Table 2. The magenta squares represent the measurements of $\mathcal{F}_\mathrm{p}$ during the time of the compression region (CR) on 2020-09-06.
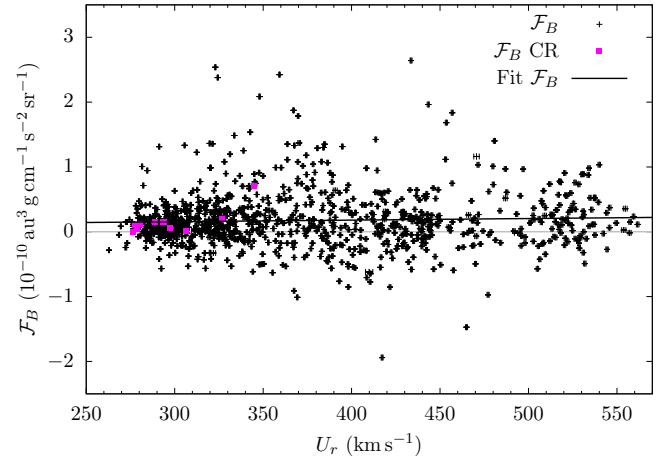
Fig. 5. Dependence of the magnetic-field contribution $\mathcal{F}_B$ to the angular-momentum flux on the radial proton bulk speed U_r. We show the measurements of $\mathcal{F}_B$ as points and overplot the linear fit to Eq. (5) as a black line. All measurement points have horizontal and vertical error bars, which are small due to the time-averaging. The fit parameters are given in Table 2. The magenta squares represent the measurements of $\mathcal{F}_B$ during the time of the compression region (CR) on 2020-09-06.

used in our study otherwise. This choice allows us to explore the variability of $\mathcal{F}_\mathrm{p}$ and $\mathcal{F}_B$ over a wider range of frequencies. Figure 7 shows the resulting power spectral densities (PSDs) of $\mathcal{F}_\mathrm{p}$ and $\mathcal{F}_B$ as functions of frequency ν.

We observe a spectral break in the PSDs of both contributions to the angular-momentum flux near a frequency of $\nu \approx 10^{-5}$ Hz. We perform separate power-law fits to PSD($\mathcal{F}_\mathrm{p}$) and PSD($\mathcal{F}_B$) on both sides of their spectral breakpoints. We find PSD($\mathcal{F}_\mathrm{p}$) $\propto \nu^{-0.45\pm0.12}$ in the low-ν regime and PSD($\mathcal{F}_\mathrm{p}$) $\propto \nu^{-1.448\pm0.012}$ in the high-ν regime. Likewise, PSD($\mathcal{F}_B$) $\propto \nu^{-0.49\pm0.14}$ in the low-ν regime and PSD($\mathcal{F}_B$) $\propto \nu^{-1.377\pm0.012}$ in the high-ν regime. We overplot the fit results in Fig. 7.

4. Discussion

Our measurements of $|\mathcal{F}_\mathrm{p}|$ are largely in agreement with previous measurements in the solar wind, which reveal values of about $4.4 \ldots 5.9 \times 10^{-11}$ au^3 g cm^{-1} s^{-2} sr^{-1} (Pizzo et al. 1983),

Table 2. Results of our linear fits to the U_r-dependence of $\mathcal{F}_\mathrm{p}$, $\mathcal{F}_B$, and $\mathcal{F}_\mathrm{tot}$ according to Eq. (5).

	a (10^{-17} au^3 g cm^{-2} s^{-1} sr^{-1})	b (10^{-9} au^3 g cm^{-1} s^{-2} sr^{-1})
$\mathcal{F}_\mathrm{p}$	-3.86 ± 0.32	1.45 ± 0.12
$\mathcal{F}_B$	0.024 ± 0.017	0.0082 ± 0.0065
$\mathcal{F}_\mathrm{tot}$	-3.84 ± 0.32	1.45 ± 0.12

$4.4 \ldots 11.2 \times 10^{-11}$ au^3 g cm^{-1} s^{-2} sr^{-1} (Finley et al. 2020), and $1.09 \ldots 2.43 \times 10^{-10}$ au^3 g cm^{-1} s^{-2} sr^{-1} (Liu et al. 2021) as averages over their whole datasets.

As shown in Sect. 3.3, we find a general trend of decreasing $\mathcal{F}_\mathrm{p}$ with increasing U_r, consistent with previous findings in data from Wind and Parker Solar Probe (Finley et al. 2019, 2020, 2021) and with estimates based on the observation of the Earth's magnetotail deflection (Němeček et al. 2020). The observation
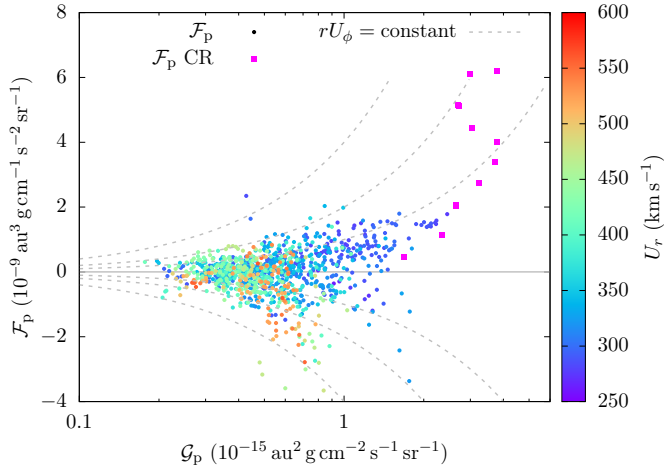
Fig. 6. Dependence of the proton contribution $\mathcal{F}_p$ to the angular-momentum flux on the radial proton mass flux $\mathcal{G}_p$. The point colour represents the value of U_r for each measurement. The magenta squares represent measurements during the time of the compression region (CR) on 2020-09-06. The grey dashed curves indicate contours of constant rU_ϕ.
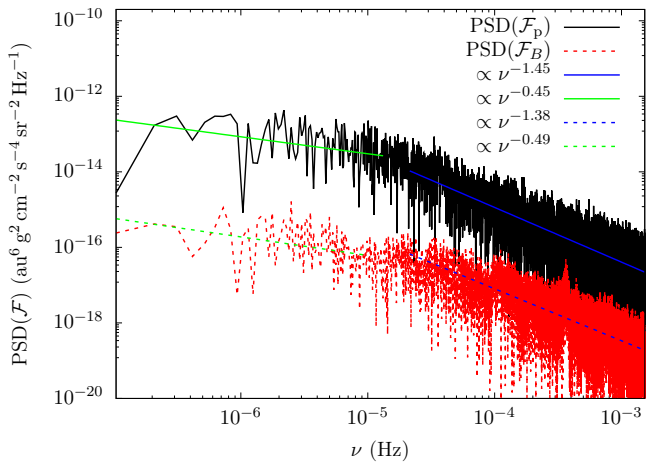

Fig. 7. Power spectral densities (PSDs) of $\mathcal{F}_p$ and $\mathcal{F}_B$. The straight lines show power-law fits of the partial spectra of $\mathcal{F}_p$ and $\mathcal{F}_B$.

of this trend in near-Sun data suggests that the trend is generated close to the Sun and not by local deflections at large distances. On average, $\mathcal{F}_p > 0$ for $U_r \lesssim 376\,\mathrm{km\,s^{-1}}$ and $\mathcal{F}_p < 0$ for $U_r \gtrsim 376\,\mathrm{km\,s^{-1}}$ according to our fit result applied to the data shown in Fig. 4. The magnetic-field contribution $\mathcal{F}_B$ shows only a small dependence on U_r, which is consistent with recent measurements from Parker Solar Probe (Liu et al. 2021).

Averaged over very long timescales, we expect both the particle contribution and the magnetic-field contribution to the angular-momentum flux to be positive due to the Sun's sense of rotation and the direction of the average Parker (1958) field. In addition, we anticipate an overall loss of the Sun's angular momentum based on observed trends in the rotation periods of Sun-like stars, which decrease with age along the main sequence. This finding is generally interpreted as a consequence of magnetised stellar winds (Lorenzo-Oliveira et al. 2019; do Nascimento et al. 2020). In the Sun's specific case, a positive net $\mathcal{F}_{tot}$ corresponds to a net loss of the Sun's rotational angular momentum.

Moreover, we expect the average relative contribution of $\mathcal{F}_B$ to the total angular-momentum flux to decrease slightly with increasing heliocentric distance as magnetic stress is converted into particle angular momentum (Weber & Davis 1967), although Marsch & Richter (1984) do not find clear evidence for this behaviour within 1 au. Previous measurements of $\mathcal{F}_B$ reveal values of about $4.1 \ldots 4.7 \times 10^{-11}\,\mathrm{au^3\,g\,cm^{-1}\,s^{-2}\,sr^{-1}}$ (Pizzo et al. 1983), $3.6 \ldots 4.7 \times 10^{-11}\,\mathrm{au^3\,g\,cm^{-1}\,s^{-2}\,sr^{-1}}$ (Finley et al. 2020), and $2.1 \ldots 3.8 \times 10^{-11}\,\mathrm{au^3\,g\,cm^{-1}\,s^{-2}\,sr^{-1}}$ (Liu et al. 2021) as the averages over their whole datasets at small heliocentric distances. These values are indeed greater than our mean values measured at Solar Orbiter's distances from the Sun, consistent with an average transfer of angular momentum from the field to the particles taking place between 0.3 and 0.7 au. Averaged over two solar cycles, Finley et al. (2019) find $\mathcal{F}_B \approx 3.58 \times 10^{-11}\,\mathrm{au^3\,g\,cm^{-1}\,s^{-2}\,sr^{-1}}$ in data from the Wind spacecraft at 1 au. Comparing to the averages at small heliocentric distances, this 1 au long-term average is also consistent with an overall decreasing trend of $\mathcal{F}_B$ with increasing r. We note, however, that our average $\mathcal{F}_B$ at intermediate distances is even smaller than the 1 au long-term average from Wind. This discrepancy is probably the result of the limited statistics in our dataset and the specific solar wind streams encountered by Solar Orbiter during its first orbit at this particular phase of the solar cycle. Radial alignments between Solar Orbiter, Parker Solar Probe, and potentially other assets with suitable pointing accuracy and instrumentation will help us to understand the partition of the contributions to the angular-momentum flux over longer time intervals in the future. In general, we expect a significant dependence of the angular-momentum flux on the Sun's 11-year activity cycle based on changes to the global magnetic field strength and changing solar-wind source regions (Finley et al. 2018).

Notwithstanding these expectations regarding large-scale behaviour, our measurements reveal the large variation of the angular-momentum flux over many timescales, from a few hours to months. Taking our full measurement time interval into account, the relative variations in $\mathcal{F}_p$ are greater than the relative variations in $\mathcal{F}_B$. When separating fast and slow wind, however, the relative variations in $\mathcal{F}_B$ are greater than those in $\mathcal{F}_p$ both in the intervals with slow ($U_r < 400\,\mathrm{km\,s^{-1}}$) and in the intervals with fast ($U_r > 500\,\mathrm{km\,s^{-1}}$) solar wind. A potential reason for this behaviour lies in the fact that $\mathcal{F}_B$ does not directly depend on U_r, while $\mathcal{F}_p$ changes significantly with U_r (see Figs. 4 and 5). We attribute the natural variations in the angular-momentum flux to changes in the solar-wind source regions (Schwenn 2006; Tindale & Chapman 2017), deflections during the expansion (Egidi et al. 1969; Siscoe et al. 1969), or large-scale fluctuations as part of the turbulent spectrum (Tu & Marsch 1995; Bruno & Carbone 2013). Furthermore, the complex field and flow geometries in the low corona and latitudinal variations of the source regions create variations in $\mathcal{F}_{tot}$ (Finley & Matt 2017; Réville & Brun 2017; Boe et al. 2020; Finley et al. 2020).

Figure 6 confirms that the scatter of data points around $\mathcal{F}_p = 0$ is more symmetric in the tenuous, low-$\mathcal{G}_p$ wind than in the denser, high-$\mathcal{G}_p$ wind. Assuming that all wind is ejected from the Sun with positive $\mathcal{F}_p$ due to the Sun's sense of rotation[2], negative $\mathcal{F}_p$ can only be created by local stream interactions, which in turn must increase $\mathcal{F}_p$ of neighbouring plasma in order to fulfil angular-momentum conservation. Our observation of a more symmetric distribution around $\mathcal{F}_p = 0$ at low $\mathcal{G}_p$ is then consistent with a scenario in which these local stream interactions

---

[2] Realistically, the possibility exists that some wind streams are initiated with $U_\phi < 0$ at the Sun.

occur more effectively in low-$\mathcal{G}_p$ wind. In this scenario, the mixing of $\mathcal{F}_p$ in low-$\mathcal{G}_p$ wind leaves the high-$\mathcal{G}_p$ wind as the main carrier of net angular-momentum flux. Figure 6 then suggests that most of the net angular-momentum flux in the solar wind is carried by dense slow wind with $\mathcal{F}_p > 0$ in the intermediate-to-high-$\mathcal{G}_p$ range.

Our spectral analysis of $\mathcal{F}_p$ and $\mathcal{F}_B$ in Sect. 3.5 quantifies the variations of the angular-momentum flux depending on the frequency, ν. The averaging time (60 min) for our analysis of the angular-momentum flux outside of Sect. 3.5 corresponds to $\nu = 2.78 \times 10^{-4}$ Hz, which lies well inside the accessible frequency range of the high-ν regime. Figure 7 does not exhibit a clear peak at the frequency associated with the Sun's equatorial rotation frequency, $\nu = \Omega_\odot/2\pi \approx 4.7 \times 10^{-7}$ Hz. The lack of such a feature suggests that the variability of the angular-momentum flux induced by repeated passes of source regions due to the Sun's rotation is negligible in our dataset. However, a spectral analysis of variations on these long timescales is not fully reliable at this stage of the mission due to the short overall duration of the dataset and its patchiness. The smallest gaps in our dataset are on order a few minutes, while the longest gap is 18 days long. We note in this context that large-scale interplanetary structures such as co-rotating interaction regions, which could be responsible for variations on these timescales, typically decay after a few revolutions. The breakpoint at $\nu \sim 10^{-5}$ Hz corresponds to a timescale of ~28 h. Assuming that this variation is frozen into the solar wind flow, this timescale corresponds to a convected length scale of ~0.27 au according to Taylor's hypothesis (Taylor 1938) based on an average $U_r \approx 400$ km s^{-1}. This scale is greater than the typical correlation length in solar wind turbulence in the inner heliosphere (Matthaeus & Goldstein 1982; Bruno & Dobrowolny 1986; Bruno & Carbone 2013; Bourouaine et al. 2020). We note, however, that the uncertainty in the visual determination of the breakpoint frequency permits values between ~6×10^{-6} Hz and ~4×10^{-5} Hz due to the noise in our Fourier spectrum. Length scales within the corresponding range of breakpoint scales are still greater than the typical correlation length. In addition, the determination of the correlation length itself is to a certain degree method-dependent. Some estimates for the correlation length of velocity fluctuations provide the same order of magnitude as the length scale associated with our breakpoint in PSD($\mathcal{F}_p$) (Podesta et al. 2008), supporting the link between fluctuations in angular-momentum flux with the turbulent fluctuations in the solar wind. It is worthwhile to perform a scale-dependent study of the angular-momentum flux in the future, in particular, by separating the variations in the low-ν regime and in the high-ν regime.

Sporadic events, such as the compression on 2020-09-06, contribute to the natural variations of the angular-momentum flux. We do not remove events like these from our statistical analysis even though they introduce a bias, as seen in Figs. 1 and 2. The on-average greater variations in slow solar wind are reflected by the greater variation of the proton contribution $\mathcal{F}_p$ to the angular-momentum flux at small U_r in Fig. 4. The mass-flux dependence of $\mathcal{F}_p$ during the time interval associated with the compression region in Fig. 6 reveals a way to separate dense intermittent structures for future analyses. Using this method, it will be interesting to investigate the contribution of co-rotating interaction regions, coronal mass ejections, and other transient mass-flux enhancements to the Sun's long-term angular-momentum loss. In fact, the amount of angular momentum carried by coronal mass ejections is still not well known. Since angular momentum is conserved, however, local angular-momentum enhancements by the deflection of background solar

wind must be balanced via flows with opposite angular momentum elsewhere in space. Figure 6 shows that the compression region in our dataset carries approximately the same specific angular momentum per proton, rU_ϕ, as the regular slow wind, yet with a higher density. This observation suggests that the compression region represents "scooped-up" solar wind mass, which has not undergone a significant alteration in terms of the particles' individual angular momentum. As shown in Fig. 5, the value of $\mathcal{F}_B$ in the compression region is comparable to the average value of $\mathcal{F}_B$ across our dataset. This observation supports our interpretation of the compression region as a density increase of otherwise unaltered background solar wind. Composition measurements of solar wind transients have the potential to confirm this interpretation in the future.

Our measurements neglect the contribution of α-particles to the angular-momentum flux. Given that their contribution to the local momentum flux is on the order of 20% (even greater near the Sun), α-particles can make a significant contribution to the total angular-momentum flux (Pizzo et al. 1983; Marsch & Richter 1984; Verscharen et al. 2015; Finley et al. 2021). Both Finley et al. (2021) and Liu et al. (2021) suggest a reconstruction of the α-particle component based on the field-alignment of the differential flow between protons and α-particles. It is still an open question, however, whether the α-particles generally serve as a net source of positive or negative angular-momentum flux. In addition, the proton beam component can carry a significant angular momentum flux (Finley et al. 2021), which we directly subsume through our using of total proton moments for ρ and U. Our analysis also neglects stresses due to pressure anisotropies in the particle populations (Hundhausen 1970; Marsch et al. 1982; Verscharen et al. 2019). This contribution to the angular-momentum flux is not significant for most of the solar wind plasma, however.

At this early stage of the mission, it is difficult to quantify the measurement uncertainties of the instruments accurately. These estimates will become more reliable as the mission progresses. At $U_r \lesssim 300$ km s^{-1}, the sensitivity of SWA/PAS decreases, so that the uncertainty in the proton moments increases. Therefore, we urge caution regarding the interpretation of the proton data (especially, the proton density) in this velocity range, which includes the compression region. Solar Orbiter's Radio and Plasma Waves (RPW, Maksimovic et al. 2020) instrument provides an estimate of the local electron density based on the probe-to-spacecraft potential and quasi-thermal noise measurements (Khotyaintsev et al. 2021), which is independent of the SWA/PAS density measurement. We find that, especially during intervals with low U_r, SWA/PAS provides a greater density value than RPW. In Appendix A, we repeat part of our analysis using the independent RPW density estimate. Although we find a reduction in the peaks of $\mathcal{F}_p$ when using the RPW density, our conclusions hold in spite of the density measurement that is applied. RPW is also able to provide an independent measurement of $|U|$ from the bias DC electric field combined with the measurement of $|B|$ from MAG. A careful cross-calibration between SWA/PAS and RPW both in terms of density and bulk-speed measurements will improve further studies in the future (Owen et al. 2020; Maksimovic et al. 2020; Walsh et al. 2020).

Early results from Parker Solar Probe report an increased azimuthal flow of the protons compared to the expectation of the Weber & Davis (1967) model at heliocentric distances up to about 0.23 au (Kasper et al. 2019). Possible explanations for this observed "angular-momentum paradox" (Réville et al. 2020) include the partitioning of angular-momentum flux between the different particle species, non-axisymmetric flows and pressure

gradients, and pressure anisotropies. In our data, however, we do not find evidence for such a persistent positive azimuthal flow. Admittedly, our data were recorded at distances greater than 0.59 au and show a different distribution of solar wind speeds compared to the study by Kasper et al. (2019). In the future, when Solar Orbiter's perihelion distance is reduced, it will be important to monitor the azimuthal flow of the protons more closely to compare with Parker Solar Probe's findings of super-rotational flows in the near-Sun solar wind.

5. Concluding remarks

A reliable quantification of the Sun's global angular-momentum loss requires measurements of the angular-momentum flux over long time intervals. In addition, we require distinctive measurements of typical equatorial and polar solar wind (McComas et al. 2000; Verscharen et al. 2021) to complete the understanding of the global angular-momentum loss. At this early point in the mission, we cannot confidently ascertain our measurement interval as a representative sample of the solar wind's angular-momentum flux. Further long-term studies will become available during Solar Orbiter's mission lifetime. At later stages of the mission, the spacecraft will leave the plane of the ecliptic making observations of the angular-momentum flux of polar solar wind feasible. Nevertheless, our study already confirms the potential for future detailed studies of the large-scale properties of the solar wind with the data from Solar Orbiter.

References

Allen, R. C., Lario, D., Odstrcil, D., et al. 2020, ApJS, 246, 36
Barnes, S. A. 2003, ApJ, 586, 464
Barnett, A. H. 2021, Appl. Comput. Harmon. Anal., 51, 1
Barnett, A. H., Magland, J. F., & Klinteberg, L. A. 2019, SIAM J. Sci. Comput., 41, C479
Boe, B., Habbal, S., & Druckmüller, M. 2020, ApJ, 895, 123
Bourouaine, S., Perez, J. C., Klein, K. G., et al. 2020, ApJ, 904, L30
Bruno, R., & Carbone, V. 2013, Liv. Rev. Sol. Phys., 10, 2
Bruno, R., & Dobrowolny, M. 1986, Annal. Geophys., 4, 17
do Nascimento, J. D., Jr., de Almeida, L., Velloso, E. N., et al. 2020, ApJ, 898, 173
Egidi, A., Pizzella, G., & Signorini, C. 1969, J. Geophys. Res., 74, 2807
Finley, A. J., & Matt, S. P. 2017, ApJ, 845, 46
Finley, A. J., Matt, S. P., & See, V. 2018, ApJ, 864, 125
Finley, A. J., Hewitt, A. L., Matt, S. P., et al. 2019, ApJ, 885, L30
Finley, A. J., Matt, S. P., Réville, V., et al. 2020, ApJ, 902, L4
Finley, A. J., McManus, M. D., Matt, S. P., et al. 2021, A&A, 650, A17
Fox, N. J., Velli, M. C., Bale, S. D., et al. 2016, Space Sci. Rev., 204, 7
Gallet, F., & Bouvier, J. 2013, A&A, 556, A36
García Marirrodriga, C., Pacros, A., Strandmoe, S., et al. 2021, A&A, 646, A121
Horbury, T. S., O'Brien, H., Carrasco Blazquez, I., et al. 2020, A&A, 642, A9
Hundhausen, A. J. 1970, Rev. Geophys. Space Phys., 8, 729
Hundhausen, A. J., Bame, S. J., Asbridge, J. R., & Sydoriak, S. J. 1970, J. Geophys. Res., 75, 4643
Kasper, J. C., Bale, S. D., Belcher, J. W., et al. 2019, Nature, 576, 228
Khotyaintsev, Yu. V., Graham, D. B., Vaivads, A., et al. 2021, A&A, 656, A19 (SO Cruise Phase SI)
Lazarus, A. J., & Goldstein, B. E. 1971, ApJ, 168, 571
Liu, Y. D., Chen, C., Stevens, M. L., & Liu, M. 2021, ApJ, 908, L41
Lorenzo-Oliveira, D., Meléndez, J., Yana Galarza, J., et al. 2019, MNRAS, 485, L68
Maksimovic, M., Bale, S. D., Chust, T., et al. 2020, A&A, 642, A12
Marsch, E., & Richter, A. K. 1984, J. Geophys. Res., 89, 5386
Marsch, E., Schwenn, R., Rosenbauer, H., et al. 1982, J. Geophys. Res., 87, 52
Matt, S. P., Brun, A. S., Baraffe, I., Bouvier, J., & Chabrier, G. 2015, ApJ, 799, L23
Matthaeus, W. H., & Goldstein, M. L. 1982, J. Geophys. Res., 87, 6011
McComas, D. J., Barraclough, B. L., Funsten, H. O., et al. 2000, J. Geophys. Res., 105, 10419
Mestel, L. 1968, MNRAS, 138, 359
Möstl, C., Weiss, A. J., Bailey, R. L., et al. 2020, ApJ, 903, 92
Müller, D., St. Cyr, O. C., Zouganelis, I., et al. 2020, A&A, 642, A1
Neugebauer, M., & Snyder, C. W. 1962, Science, 138, 1095
Němeček, Z., Ďurovcová, T., Šafránková, J., et al. 2020, ApJ, 897, L39
Owen, C. J., Bruno, R., Livi, S., et al. 2020, A&A, 642, A16
Pantolmos, G., & Matt, S. P. 2017, ApJ, 849, 83
Parker, E. N. 1958, ApJ, 128, 664
Pizzo, V., Schwenn, R., Marsch, E., et al. 1983, ApJ, 271, 335
Podesta, J. J., Galvin, A. B., & Farrugia, C. J. 2008, J. Geophys. Res.: Space Phys., 113, A09104
Reiners, A., & Mohanty, S. 2012, ApJ, 746, 43
Réville, V., & Brun, A. S. 2017, ApJ, 850, 45
Réville, V., Velli, M., Panasenco, O., et al. 2020, ApJS, 246, 24
Richter, A. K., & Luttrell, A. H. 1986, J. Geophys. Res., 91, 5873
Schwenn, R. 2006, Space Sci. Rev., 124, 51
Siscoe, G. L., Goldstein, B., & Lazarus, A. J. 1969, J. Geophys. Res., 74, 1759
Stansby, D., Horbury, T. S., & Matteini, L. 2019, MNRAS, 482, 1706
Taylor, G. I. 1938, Proc. R. Soc. London Ser. A, 164, 476
Tindale, E., & Chapman, S. C. 2017, J. Geophys. Res.: Space Phys., 122, 9824
Tu, C. Y., & Marsch, E. 1995, Space Sci. Rev., 73, 1
Verscharen, D., Chandran, B. D. G., Bourouaine, S., & Hollweg, J. V. 2015, ApJ, 806, 157
Verscharen, D., Klein, K. G., & Maruca, B. A. 2019, Liv. Rev. Sol. Phys., 16, 5
Verscharen, D., Bale, S. D., & Velli, M. 2021, MNRAS, 506, 4993
Walsh, A. P., Horbury, T. S., Maksimovic, M., et al. 2020, A&A, 642, A5
Weber, E. J., & Davis, L., Jr. 1967, ApJ, 148, 217

Appendix A: The angular-momentum and mass flux based on the RPW density

RPW measures the local total electron density n_e based on a combination of both the peak-tracking of the plasma frequency and the spacecraft potential (Khotyaintsev et al. 2021). Due to quasi-neutrality, n_e serves as an independent measure of the total charge-weighted ion density. For comparison with our SWA/PAS-MAG measurements, we create a new dataset using U from SWA/PAS, B from MAG, and $\rho = m_p n_e$ from RPW, where m_p is the proton mass. We apply the same selection, averaging, and analysis methods as in the main part of this work. This leaves us with 913 data points for our combined SWA/PAS-MAG-RPW dataset in total.

We show the timeseries of our combined SWA/PAS-MAG-RPW dataset in Fig. A.1. Qualitatively, the timeseries agrees with Fig. 1. However, the peaks with $\mathcal{F}_p > 0$ are less pronounced in the SWA/PAS-MAG-RPW dataset than in the SWA/PAS-MAG dataset. These peaks, including our compression region

on 2020-09-06, correspond to intervals of slow and dense solar wind, for which the SWA/PAS and RPW densities diverge most.

We present the statistical properties of our combined SWA/PAS-MAG-RPW dataset in Table A.1. Due to the lower peaks in $\mathcal{F}_p$, the signs of the mean values for $\mathcal{F}_p$ and $\mathcal{F}_{tot}$ across our full dataset are now different from the signs of the same quantities in the SWA/PAS-MAG dataset shown in Table 1. The maxima of $\mathcal{F}_p$ and $\mathcal{F}_{tot}$ in Table A.1 are lower than those given in Table 1, reflecting the lower peaks seen in Fig. A.1. All other statistical markers in Table A.1 agree with our results shown in Table 1.

We show the dependence of $\mathcal{F}_p$ on $\mathcal{G}_p$ for our combined SWA/PAS-MAG-RPW dataset in Fig. A.2. The comparison between Figs. 6 and A.2 shows that most high-$\mathcal{G}_p$ measurements, including the compression region, shift towards smaller values of $\mathcal{G}_p$ when using the RPW density estimate. In addition, the compression region shifts towards smaller values of $\mathcal{F}_p$. Notwithstanding these differences, our conclusions drawn based on Fig. 6 are still valid.
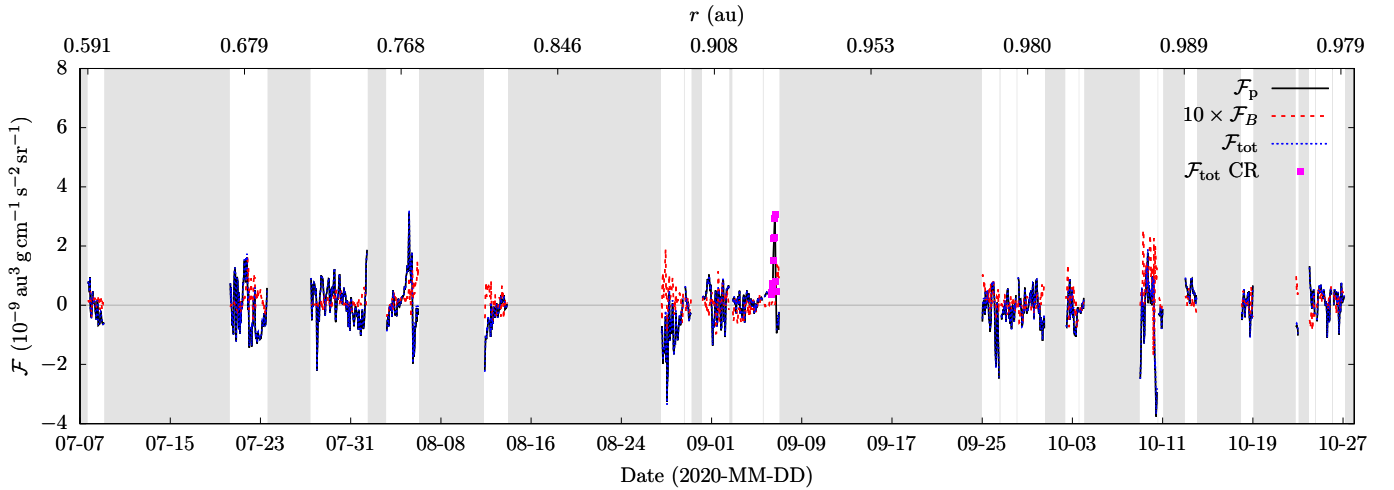

Fig. A.1. Same as Fig. 1, but using ρ from RPW in the calculation of $\mathcal{F}_p$ and $\mathcal{F}_{tot}$. The grey-shaded areas indicate times for which our merged SWA/PAS-MAG-RPW data product is unavailable or the data flags for either dataset indicate poor data quality.

Table A.1. Same as Table 1, but using ρ from RPW in the calculation of $\mathcal{F}_p$ and $\mathcal{F}_{tot}$.

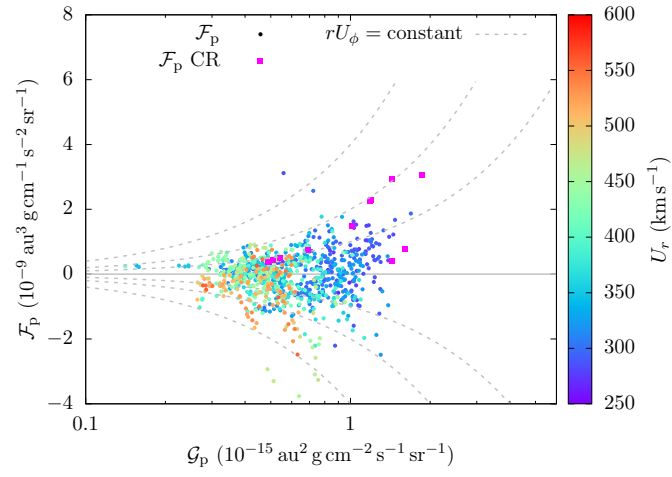|	Mean $(10^{-11}\,\mathrm{au^3\,g\,cm^{-1}\,s^{-2}\,sr^{-1}})$	Min $(10^{-9}\,\mathrm{au^3\,g\,cm^{-1}\,s^{-2}\,sr^{-1}})$	Max $(10^{-9}\,\mathrm{au^3\,g\,cm^{-1}\,s^{-2}\,sr^{-1}})$
All speeds			
$\mathcal{F}_p$	-5.33 ± 72.20	-3.76	3.12
$\mathcal{F}_B$	1.67 ± 4.24	-0.169	0.254
$\mathcal{F}_{tot}$	-3.66 ± 72.20	-3.69	3.21
$U_r < 400\,\mathrm{km\,s^{-1}}$			
$\mathcal{F}_p$	10.5 ± 70.5	-2.49	3.12
$\mathcal{F}_B$	0.735 ± 5.840	-0.230	0.254
$\mathcal{F}_{tot}$	11.2 ± 70.3	-2.49	3.21
$U_r > 500\,\mathrm{km\,s^{-1}}$			
$\mathcal{F}_p$	-67.2 ± 106.5	-5.43	0.753
$\mathcal{F}_B$	0.605 ± 5.464	-0.174	0.101
$\mathcal{F}_{tot}$	-66.6 ± 108.6	-5.57	0.836

Fig. A.2. Same as Fig. 6, but using ρ from RPW in the calculation of $\mathcal{F}_\mathrm{p}$ and $\mathcal{G}_\mathrm{p}$.